

# Conjugated Azo Compounds as Active Materials for Rechargeable Sodium-Metal Batteries with High-Rate Performance

Jiawen Wang<sup>+</sup><sup>[a]</sup> Yifan Tong<sup>+</sup><sup>[a]</sup> Weiwei Huang,<sup>\*[a]</sup> and Qichun Zhang<sup>\*[b, c]</sup>

Organic electrode materials have gained growing attention in the field of sodium-metal batteries due to their rich reserves, flexibility, and environmental friendliness. However, organic small molecules suffer from poor stability in the electrolyte leading to the decay of battery capacity and reduced cycle life. To address these issues, we report a linear polymer p-PADA with N=N and C=N as active centers. Its highly-conjugated and

polymerized structure endows the p-PADA electrode stability, faster reaction kinetics, and exceptional rate performance. When the current density reaches  $5 \text{ A g}^{-1}$ , p-PADA still exhibits a specific capacity of  $313 \text{ mAh g}^{-1}$  after 1000 cycles. This work demonstrates that polymerization is an effective method to enhance the electrochemical properties of organic materials.

## Introduction

Sodium-metal batteries (SMBs) have been widely considered as the promising candidate for LIBs, benefiting from their low cost, excellent safety, abundant sodium supplies, and similar electrochemical characteristics.<sup>[1]</sup> Unlike LIBs, SMBs are free of over-discharge, thus they can achieve maximum energy density by discharging to zero volts.<sup>[2]</sup> However, the radius of sodium ions ( $1.02 \text{ \AA}$ ) is bigger than lithium ions ( $0.76 \text{ \AA}$ ), and significant volume changes of SMBs would be encountered during the insertion/extraction of sodium ions, resulting in low specific capacity and sluggish kinetics.<sup>[3]</sup> In this situation, searching for novel SMBs electrode materials with high specific capacity and rapid ion diffusion put a positive sign in the development of efficient energy storage systems.

Currently, the electrode materials for SMBs still rely on non-renewable and expensive inorganic materials with low practical capacity and poor cycling performance, as well as irreversible volume expansion when embedded with ions.<sup>[4]</sup> In contrast, organic electrode materials feature the advantages of environmental friendliness, abundant storage, and inexpensive nature,

and their good flexibility allows them to accommodate larger sodium ions without significant volume expansion.<sup>[5]</sup> More importantly, the designability of organic molecules facilitates the directional design and functionalization of electrodes.<sup>[6]</sup> However, organic electrode materials also suffer from some defects, for example, organic small molecule materials usually cause rapid deterioration of battery capacity and lifespan decay due to their high solubility.<sup>[7]</sup>

Polymerization has been recognized as an effective method to inhibit the dissolution of organic materials in the electrolyte and improve the cycle lifespan of batteries.<sup>[8]</sup> In addition, the introduction of conjugate structures and redox functional groups in polymers contributes the improvement of cyclic stability and provides rapid reaction kinetics.<sup>[9]</sup> N=N, as a highly active functional group for metal ion storage, has been demonstrated for reversible binding to sodium ions in SMBs.<sup>[10]</sup> In 2018, Wang groups demonstrated for the inaugural time that N=N groups can be treated as electrochemically-active centers for ion storage, commencing the exploration of azo molecules as electrochemical materials.<sup>[11]</sup> Shortly thereafter, the first application of highly porous azo-linked polymers (ALPs) as electrode materials for SMBs was carried out by Kaderi et al. and a good specific capacity of  $170 \text{ mAh g}^{-1}$  could be obtained at  $0.3 \text{ C}$ .<sup>[12]</sup>

Based on previous work,<sup>[13]</sup> we herein selected N=N and C=N as the redox cores and synthesized the conjugated linear polymer terephthalaldehyde-4,4'-diazoaniline (p-PADA) as the electrode material for SMBs via the simple Schiff base reaction of terephthalaldehyde (PA) with 4,4'-diazoaniline (Azo). Its electrochemical properties were compared with those of benzaldehyde-4,4'-diazoanilidene (BADA), a small molecule compound with the same repeating unit synthesized via benzaldehyde (BA) with Azo. As expected, the linear polymer is nearly insoluble in the electrolyte with better cycling stability and demonstrates superior electrochemical kinetics and rate performance. This stems from the fact that polymerization extends the  $\pi$ -conjugated structure, resulting in an effective

[a] J. Wang,<sup>+</sup> Dr. Y. Tong,<sup>+</sup> Prof. W. Huang  
Hebei Key Laboratory of Applied Chemistry  
Yanshan University  
Qinhuangdao 066004, China  
E-mail: qiczhang@cityu.edu.hk  
huangweiwei@ysu.edu.cn

[b] Prof. Q. Zhang  
Department of Materials Science and Engineering  
City University of Hong Kong  
Hong Kong SAR 999077, China

[c] Prof. Q. Zhang  
Center of Super-Diamond and Advanced Films (COSDAF)  
City University of Hong Kong  
Hong Kong SAR 999077, China

<sup>†</sup> These authors contributed equally to this work.

Supporting information for this article is available on the WWW under  
<https://doi.org/10.1002/batt.202200413>

An invited contribution to a Special Collection on Organic Batteries

improvement in the electrochemical properties of the polymer.<sup>[14]</sup> Meanwhile, the co-modification of electrochemical activity of p-PADA by the C=N and N=N promotes the storage of sodium ions, allowing the battery to achieve high capacity. At a high current density of  $5 \text{ A g}^{-1}$ , the specific capacity of the p-PADA battery is available up to  $400 \text{ mAh g}^{-1}$ , substantially higher than BADA ( $264 \text{ mAh g}^{-1}$ ). Its excellent cycling capability allows it to maintain a specific capacity of  $313 \text{ mAh g}^{-1}$  after 1000 cycles. This further proves that polymerization and increased conjugation can significantly improve the electrochemical properties of organic materials.

## Results and Discussion

The synthetic routes of benzaldehyde-4,4'-diazooanilidine (BADA) and terephthalaldehyde-4,4'-diazooanilidine (p-PADA) are illuminated in Figure 1(a), where the specific synthesis conditions have been provided at the end of this article. The difference between BADA and p-PADA is that the polymerization endows p-PADA with a linear and extended  $\pi$ -conjugated structure. The highest occupied molecular orbital (HOMO) and the lowest unoccupied molecular orbital (LUMO) energy levels for the repeating units of both substances have been calculated to understand the influence of chemical structure on the electronic structure, where a narrower LUMO-HOMO gap ( $E_g$ ) corresponds to better conductivity.<sup>[15]</sup> Judging from Figure 1(b), the  $E_g$  value of p-PADA (2.7 eV) is lower than for BADA (3.2 eV) due to the extended structure of the p-PADA conjugated systems promoting electron delocalization and enhancing conductivity.<sup>[16]</sup>

Fourier-transform infrared spectroscopy (FTIR) spectra of p-PADA, BADA, and their monomers are presented in Figure 2(a). A peak at  $1578 \text{ cm}^{-1}$  belonging to N=N was observed in Azo, BADA, and p-PADA.<sup>[17]</sup> For monomer Azo, the peak at  $3375 \text{ cm}^{-1}$  comes from the stretching vibration of N–H bonds, which disappears in BADA/p-PADA.<sup>[18]</sup> Instead, new peaks at  $1621 \text{ cm}^{-1}$  (assigning to C=N bonds) were observed for both materials, while the peaks in PA belonging to C=O at  $1695 \text{ cm}^{-1}$  are weakened, demonstrating the successful synthesis of both materials.<sup>[19]</sup> Considering that BADA is extremely soluble in dimethyl sulfoxide (DMSO), its structure was determined by  $^1\text{H}$  NMR spectroscopy. Conversely, p-PADA is not soluble in conventional organic solvents, and for this reason, selecting solid-state  $^{13}\text{C}$  magic-angle spinning Nuclear Magnetic Resonance Spectroscopy (NMR) has been conducted to ascertain its structure. In the

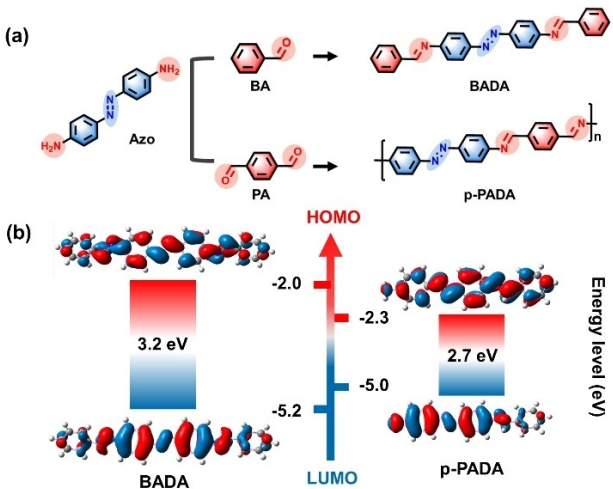


Figure 1. a) Synthetic routes to BADA and p-PADA. b) HOMO and LUMO energy levels of BADA and p-PADA.

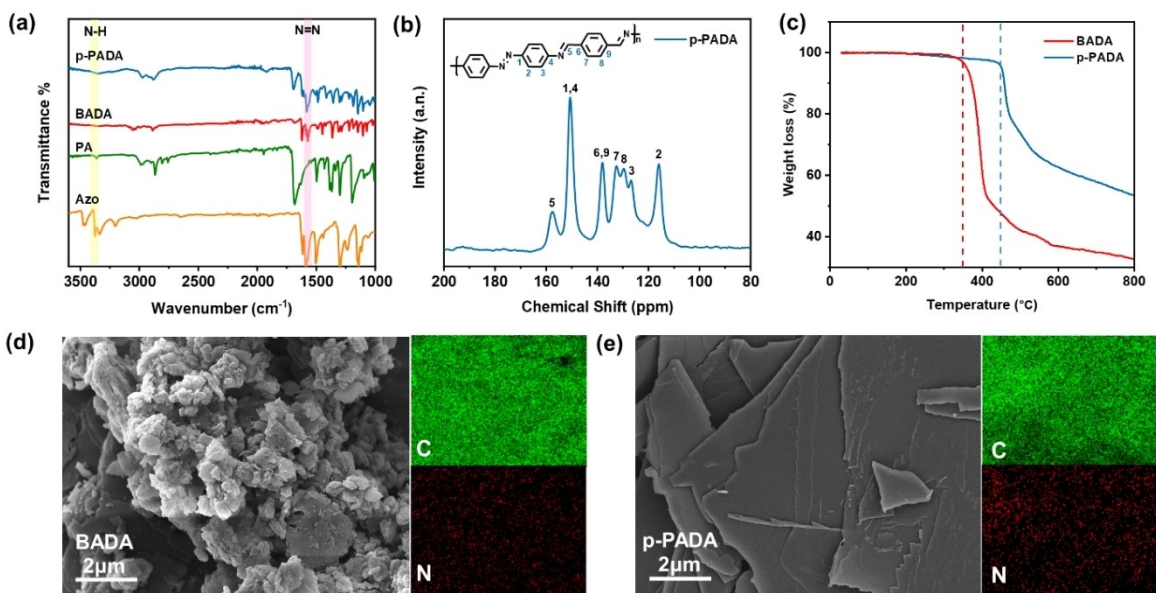


Figure 2. a) FTIR spectra of Azo, PA, BADA, and p-PADA. b)  $^{13}\text{C}$  NMR solid-state spectrum of p-PADA. c) Thermogravimetric analysis curves of p-PADA and BADA. d) SEM images and element mappings (C and N) of BADA. e) SEM images and element mappings (C and N) of p-PADA.

<sup>13</sup>C NMR spectrum (Figure 2b), the signal located at 157.60 ppm confirms the formation of the C=N bond,<sup>[20]</sup> and the response signal at 150.52 ppm is from the C in C–N bond. The different H atoms of BADA have been labeled separately in the spectra of Figure S1. The scanning electron microscope (SEM) was carried out to investigate the surface morphology of BADA and p-PADA (Figure 2d and e). BADA showed a disordered stacking state while a clear nanosheet stacking structure could be observed for the p-PADA sample, which facilitated the rapid penetration of the electrolyte. Also, the Energy Dispersive Spectroscopy (EDS) mapping suggests the uniform distribution of different elements (C, N). The thermal stabilities of BADA and p-PADA were investigated by thermogravimetric analysis in N<sub>2</sub> atmosphere. Apparently, p-PADA has inconspicuous decomposition until 450 °C (Figure 2c), indicating that its thermal stability is better than that of BADA (noticeable weight loss at 350 °C).

In order to investigate the sodium storage behavior of these two materials, 1 M NaPF<sub>6</sub> in DIGLYME (vol 100%) was selected as the electrolyte, and 50 wt% BADA/p-PADA, 40 wt% Ketjen black, and 10 wt% polyvinylidene fluoride (PVDF) were used to fabricate the composite electrode. A CR2032 coin-shaped cell was fabricated with sodium metal foil as a counter electrode. Cyclic voltammetry (CV) tests were conducted at a scan rate of 0.5 mV s<sup>-1</sup> over a voltage range of 0.01–3 V (Figures 3a, S2 and S3). In the initial cycle (Figure 3a), a cathode peak can be found at 0.82 V, which vanishes in the subsequent scanning. This is due to the solid electrolyte interface (SEI) formation. Four different pairs of redox peaks can be noticed at 0.48/0.35 V, 0.95/1.13 V, 1.40/

1.24 V, and 1.74/1.41 V in the subsequent cycles, corresponding to a multi-step sodium ion embedding process.<sup>[21]</sup> During cycles, the gradual reduction of the anode peak current and the shift with cycling in 0.01–1 V are related to the presence of irreversible reactions inside the cell.<sup>[22]</sup> Meanwhile, no obvious plateaus are observed in the GCD curves (Figures 3b and S4), implying a possible multiple sodium storage process.<sup>[23]</sup> This phenomenon may arise from the continuous procedures of reduction/oxidation of dual-site C=N and N=N generating unobvious and indiscernible discharge and charge plateaus.<sup>[24]</sup>

The rate performance at varied current rates of p-PADA was also evaluated to pursue the influence of conjugated polymers on the electrochemical properties. As displayed in Figure 3(c), p-PADA can deliver high reversible capacities of 553.5, 353.0, 330.5, 318.6, 308.5, 301.5, and 294.2 mAh g<sup>-1</sup> at current densities of 0.1, 0.2, 0.5, 1, 2, 3 and 5 Ag<sup>-1</sup>, respectively, significantly higher than those of BADA. Even if the current density returns to 0.1 Ag<sup>-1</sup>, the p-PADA can still restore the initial reversible capacity without fading. Stable rate performance implies that the extended π-conjugated structure enables higher stability of p-PADA in the process of repeated sodiation/desodiation, resulting in superior reversibility and reaction kinetics.<sup>[25]</sup>

The excellent cycling stability of p-PADA electrode is also verified by the cycling tests. As displayed in Figure 3(d), the discharge specific capacity of p-PADA/BADA decreases and then increases in the preliminary stage, and the capacity remains stable in subsequent cycles. This process can be attributed to the gradual penetration of the electrolyte and the slow but continuous electrochemical activation process during the cycling.<sup>[26]</sup> At a current density of 5 Ag<sup>-1</sup>, BADA can obtain a reversible capacity of 267 mAh g<sup>-1</sup>, while p-PADA could achieve a high reversible capacity of 400 mAh g<sup>-1</sup>, retaining 313 mAh g<sup>-1</sup> even after 1000 cycles, much higher than BA (22.5 mAh g<sup>-1</sup>). The high solubility of BADA in the electrolyte causes its specific capacity to decay sharply during cycling. In comparison, the outstanding cycle life with better cycle stability of p-PADA is primarily attributed to its excellent insolubility during the process of electrochemical cycling. The insolubility of BADA and p-PADA have been compared through solubility experiments in the electrolyte. As depicted in Figure S5, we immersed BADA and p-PADA in the DIGLYME electrolyte for 1, 15, and 30 days to visualize their dissolution states, respectively. The electrolyte soaked with BADA turned yellow immediately after addition and became darker and darker with time, and was orange-yellow after 30 days. Instead, the electrolyte soaked with p-PADA has no significant color change in 30 days. This phenomenon suggests that the solid backbone of p-PADA and the large planar conjugated system can inhibit dissolution.<sup>[27]</sup> The BADA/p-PADA batteries were disassembled and the morphological changes of the electrode sheets before and after cycling were observed by SEM (Figure S6), the surface morphology of BADA/p-PADA becomes smoother and flatter after cycling.

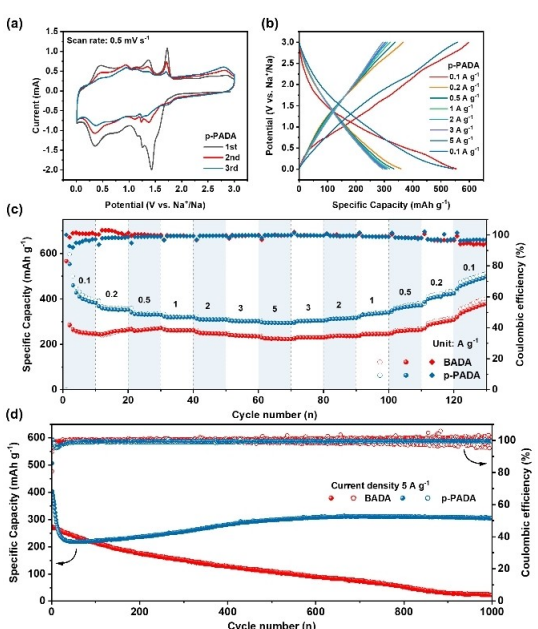


**Figure 3.** a) CV profiles of p-PADA composite electrodes at a scan rate of 0.5 mV s<sup>-1</sup>. The composite electrodes were made in the ratio of p-PADA: Ketjen black: PVDF = 5:4:1. b) Galvanostatic charging-discharging curves of p-PADA. c) Rate performances of BADA and p-PADA. d) Cycle performances of BADA and p-PADA at 5 Ag<sup>-1</sup>.

Cyclic voltammetry (CV) at different scan rates, Galvanostatic Intermittent Titration Technique (GITT) tests, and electrochemical impedance spectroscopy (EIS) were performed to further investigate the reaction kinetics of p-PADA in sodium-metal batteries. With increasing scan rate, the CV curves keep a similar shape, however, the current density of the characteristic peaks continuously varies (Figures 4a and S7), which can be due to the transition from the diffusion control mechanism to the capacitive control mechanism during cycling.<sup>[28]</sup> According to the power law, the relationship between scan rate ( $v$ ) and current ( $i$ ) is given by the following equation:

$$i = av^b$$

where  $a$  and  $b$  are variable parameters. When the  $b$  value is around 0.5, the electrochemical process of the cell is mainly controlled by diffusion. When the  $b$  value is close to 1.0, the reaction process is mainly controlled by capacitance.<sup>[29]</sup> The linear fit of the natural logarithm of the current versus the scan rate was plotted in Figure 4(b). The  $b$  values of peaks A–G are 0.57, 0.63, 0.61, 0.82, 0.68, 0.78, and 0.64, respectively, so the reaction kinetics of the p-PADA electrode is determined by the combination of sodium ion diffusion control and capacitance control. Figure S8 also gives the  $b$ -value analysis of BADA. Unlike p-PADA, the reaction kinetics of BADA is mainly dominated by sodium ion diffusion. Figure 4(c) shows the contributions of pseudo-capacitance and diffusion-controlled charge storage of p-PADA, where the contribution of the capacitive behavior is 52% for a scan rate of  $0.2 \text{ mV s}^{-1}$ . The percentage of capacitance contribution increases significantly with the scanning rate in the p-PADA electrode, implying that the storage of sodium ions in

the p-PADA is a fast-moving pseudo-capacitance process.<sup>[30]</sup> To further explore the diffusion mechanism of sodium ions and the discrepancy in reaction kinetics between the two electrodes, GITT analysis was performed at  $0.1 \text{ A g}^{-1}$  (Figures 4d and S9). The sodium ion diffusion coefficient ( $D_{\text{Na}^+}$ ) can be calculated by:

$$D_{\text{Na}^+} = \frac{4}{\pi \tau} \left( \frac{m_B V_M}{M_B A} \right)^2 \left( \frac{\Delta E_s}{\Delta E_t} \right)^2$$

where  $m_B$ ,  $V_M$ , and  $M_B$  represent the mass, molar volume, and molecular weight of the active material, respectively.  $A$  represents the contact area between the active material and electrolyte,  $\tau$  is the duration of the current pulse, and  $\Delta E_s$  and  $\Delta E_t$  are the changes in equilibrium potential and voltage, respectively.<sup>[31]</sup> In Figure 4(e), the  $D_{\text{Na}^+}$  values of the charging process are higher than those of the discharging process since there is an activation process in the p-PADA. The average sodium-ion diffusion coefficient ( $D_{\text{Na}^+}$ ) of p-PADA is  $\approx 2.12 \times 10^{-10} \text{ cm}^2 \text{s}^{-1}$ , which is obviously higher than BADA ( $D_{\text{Na}^+} \approx 1.43 \times 10^{-10} \text{ cm}^2 \text{s}^{-1}$ , Figure S10). Clearly, these results suggest that p-PADA electrode has a faster electrochemical reaction kinetics, which is mainly because the extended conjugate structure ensures the rapid diffusion of sodium ions.<sup>[32]</sup>

The fitting results of EIS data using the equivalent circuit (Figure S11) have been given in Table S1. In Figure S12, the initial charge transfer resistances of BADA and p-PADA were  $54.63 \Omega$  and  $44.36 \Omega$ , respectively. The smaller charge transfer resistance indicates the higher conductivity and faster electron transfer rate of p-PADA than BADA.<sup>[33]</sup> Figure 4(f) shows the electrochemical impedance properties of the recovered electrodes after a different number of cycles when

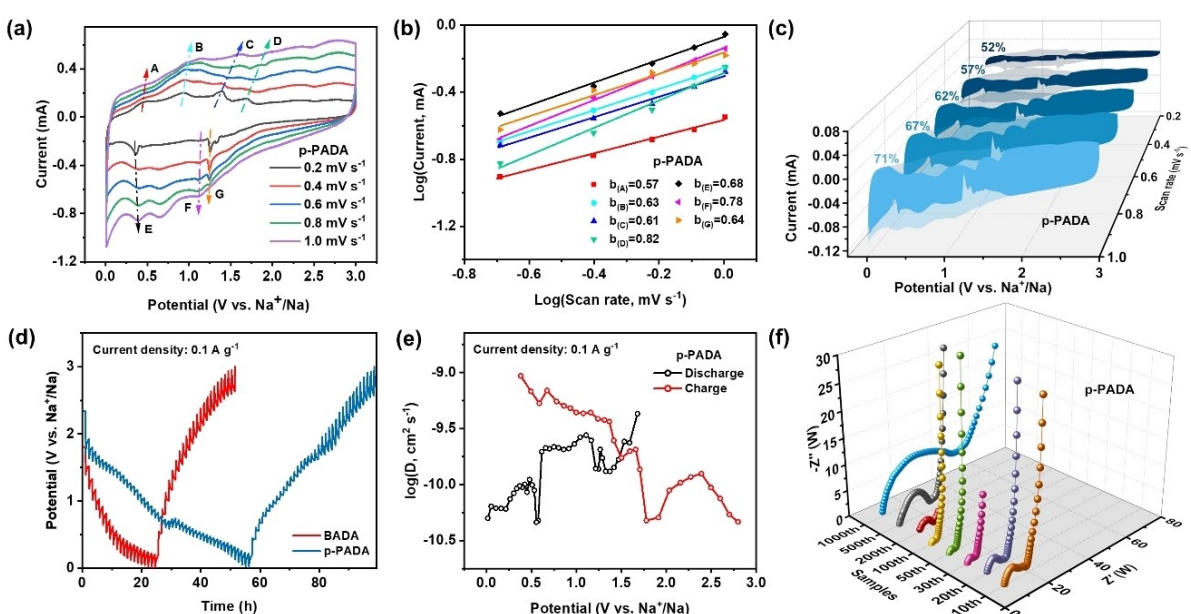


**Figure 4.** a) CV curves of p-PADA at different scan rates. b) b-Value analysis of p-PADA using the relationship between the peak currents and scan rates. c) The contribution ratio of p-PADA's capacitive capacities and diffusion-controlled capacities at different scan rates. d) GITT curves at  $0.1 \text{ A g}^{-1}$  of BADA and p-PADA. e)  $\text{Na}^+$  diffusion coefficients of p-PADA at  $0.1 \text{ A g}^{-1}$ . f) The Impedance of different cycles of p-PADA.

the current density is  $5 \text{ A g}^{-1}$ . The charge transfer resistance of the p-PADA decreases with the number of cycles and gradually increases again after 100 cycles, indicating a gradual activation process during cycling performance,<sup>[34]</sup> while the interfacial impedance of BADA kept changing with increasing cycles (Figure S13). These results suggest that, since small molecules are easily soluble in electrolytes, their stability in electrodes during electrochemical process becomes much worse comparing to that of polymers.

To explore the energy storage mechanism of p-PADA, *ex-situ* IR spectroscopy test has been conducted. As shown in Figure 5(a), the peaks located at  $1631 \text{ cm}^{-1}$  and  $1578 \text{ cm}^{-1}$  can be assigned to C=N and N=N, respectively.<sup>[13,17]</sup> During the sodiation of p-PADA (from 3 V to 0.01 V discharge), a gradual weakening of both peaks of N=N and C=N groups can be observed, probably due to the fact that N=N and C=N have been converted into N–N and C–N. These results illustrated that N=N and C=N groups have been successively intercalated with sodium ions. Subsequently charging from 0.01 V to 3 V, both characteristic peaks of C=N and N=N recovered during the desodiation, accounting for the reversible storage of sodium ions in C=N and N=N sites.<sup>[35]</sup> Based on these variations of N=N and C=N and the previous reports,<sup>[36]</sup> the sodium ion storage mechanism of p-PADA can be speculated as four sodium ions on each repeating unit and the possible reaction mechanism has been proposed in Figure 5(b).

## Conclusion

In summary, a small molecule compound BADA and a polymer p-PADA containing similar active units were synthesized and applied as electrode materials for SMBs. From computational and experimental results, p-PADA exhibits more stable rate performance and cycling stability than BADA. At a high current density of  $5 \text{ A g}^{-1}$ , p-PADA was able to maintain a high specific capacity of  $313 \text{ mAh g}^{-1}$  after 1000 cycles, which is attributed to the polymerization that can extend the  $\pi$ -conjugated structure, improve the electrochemical properties, and promote

fast electron transfer. The EIS and GITT further confirm the rapidly-responsive ability of p-PADA to kinetics. This research proves that rational molecular design and polymerization can significantly strengthen the electrochemical performance of SMBs.

## Experimental Section

### Materials

All reagents including 4,4'-diamoaniline (Azo), benzaldehyde (BA), and terephthalic dialdehyde (PA) were purchased from Aladdin Biochemical Technology Co. and were able to be used directly in the reactions without further purification. Ketjen black was purchased from Delta Biologics Ltd. 1 M NaPF<sub>6</sub> in DIGLYME (vol 100%) was purchased from DoDo Chem.

### Synthesis of BADA

Under nitrogen atmosphere, Azo (6 mmol), acetic acid (4 mL), anhydrous ethanol (100 mL), and BA (12 mmol) were added to a 250 mL flask. The mixture was heated in an oil bath at 90 °C for 12 hours. The resulting solid product was collected after cooling. Then, the mixture was washed with ethanol and dried under vacuum to finally obtain a light orange solid. <sup>1</sup>H NMR (600 MHz, DMSO-d<sub>6</sub>): δ = 8.74 (s, 2H), 7.99 (s, 10H), 7.56 (s, 4H), 7.47 (s, 4H).

### Synthesis of p-PADA

A mixture of Azo (2 mmol), acetic acid (4 mL), and 40 mL DMF was heated in an oil bath to 140 °C until the azo solid was no longer observed. Subsequently, PA (2 mmol) was added to the mixed solution and the resulting mixture was refluxed at 140 °C under N<sub>2</sub> atmosphere for 24 h. After naturally cooling down to room temperature, the resulting precipitate was washed with methanol and acetone, respectively. The pure p-PADA orange powder was obtained after drying at 60 °C overnight.

### Material characterizations

Fourier-transform infrared spectroscopy (FTIR; FTIR650 spectrometer), <sup>1</sup>H nuclear magnetic resonance (<sup>1</sup>H NMR, 600 Hz), and solid-state <sup>13</sup>C cross-polarization magic-angle spinning spectroscopy (Bruker 400 MHz NMR) were used to determine the structure of BADA and p-PADA. The thermal stability of both materials was characterized by thermogravimetric analysis (TGA, Agilent DD2 Belsorp Max) under Ar atmosphere. The morphologies of the p-PADA and BADA materials and the relevant electrodes were observed by scanning electron microscopy (SEM; Zeiss Merlin Compact). Energy dispersive spectroscopy (EDS) of the P-PADA and BADA and the relevant electrodes before and after discharge/charge were characterized by Zeiss Merlin Compact.

### Electrochemical measurements

All electrochemical tests were conducted using the CR2032 coin cells, where sodium foils were used as the counter electrode, glass microfiber membranes (Celgard 2400 membrane separator) as the separators, and 1 M NaPF<sub>6</sub> in DIGLYME (vol 100%) solution as the electrolyte. BADA/p-PADA electrodes were prepared as follows: 50 wt% BADA/p-PADA powder, 40 wt% Ketjen black,

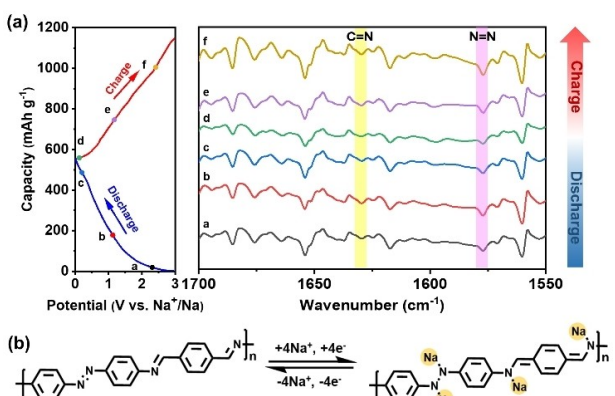


Figure 5. a) The ex-situ FTIR spectra of p-PADA. b) Structural evolution of p-PADA during redox sodiation.

and 10 wt% polyvinylidene fluoride (PVDF) were mixed and dispersed in N-methyl-2-pyrrolidone (NMP), and the resulting slurry was uniformly coated on the copper foils and then dried in vacuum at 60 °C for 12 h. Finally, the copper foils were stamped into discs with a diameter of 12 mm, and the cells were prepared in the glovebox filled with Ar. The active material loading was found to be ~0.5 mg cm<sup>-2</sup>. GCD was performed on the Neware CT-4008T with a voltage range of 0.01–3.0 V. CV and EIS were carried out on the electrochemical workstation (CHI-660E), where the scan rate of CV was 0.5 mVs<sup>-1</sup> and the voltage range was 0.01–3 V. All the tests were conducted at 25 °C. The capacity contribution of Ketjen black is given in the Supporting Information (Figure S14).

### Density functional theory calculations

On the basis of density functional theory (DFT) using the B3LYP method with 6-311G(d,p) basic sets, the Gaussian 16 package is chosen to calculate the distribution of the highest occupied molecular orbital (HOMO) and the lowest unoccupied molecular orbital (LUMO) and their electron clouds for two molecules.

### Acknowledgements

This study was financially supported by the National Natural Science Foundation of China (Nos. 21875206, 21403187) and the Subsidy for Hebei Key Laboratory of Applied Chemistry after Operation Performance (Nos. 22567616H). Q.Z. thanks the funding support from City University of Hong Kong (9380117, 7005620 and 7020040) and Hong Kong Institute for Advanced Study, City University of Hong Kong, Hong Kong, P. R. China.

### Conflict of Interest

The authors declare no conflict of interest.

### Data Availability Statement

The data that support the findings of this study are available in the supplementary material of this article.

**Keywords:** anode materials • azo-linked polymers • electrochemical energy storage • organic electrodes • sodium-metal batteries

- [1] a) S.-X. Xia, Y.-H. Yan, H. Sun, J.-H. Yang, S.-Y. Zheng, *Rare Met.* **2022**, *41*, 1496–1503; b) J. Li, C. Han, X. Ou, Y. Tang, *Angew. Chem. Int. Ed. Engl.* **2022**, *61*, e202116668; c) C.-X. Xu, J.-J. Jiang, *Rare Met.* **2020**, *40*, 243–245.
- [2] a) X. Yin, S. Sarkar, S. Shi, Q. A. Huang, H. Zhao, L. Yan, Y. Zhao, J. Zhang, *Adv. Funct. Mater.* **2020**, *30*, 1908445; b) Y.-F. Zhu, Y. Xiao, S.-X. Dou, Y.-M. Kang, S.-L. Chou, *eScience* **2021**, *1*, 13–27; c) M. Zhang, Y. Tong, J. Xie, W. Huang, Q. Zhang, *Chem. Eur. J.* **2021**, *27*, 16754–16759; d) W. Xiong, W. Huang, M. Zhang, P. Hu, H. Cui, Q. Zhang, *Chem. Mater.* **2019**, *31*, 8069–8075; e) S. Wang, C. Sun, N. Wang, Q. Zhang, *J. Mater. Chem. A* **2019**, *7*, 10138–10158.

- [3] Y. Pang, H. Li, S. Zhang, Q. Ma, P. Xiong, R. Wang, Y. Zhai, H. Li, H. Kang, Y. Liu, L. Zhang, L. Zhang, T. Zhou, C. Zhang, *J. Mater. Chem. A* **2022**, *10*, 1514–1521.
- [4] J. Zhao, M. Zhou, J. Chen, L. Tao, Q. Zhang, Z. Li, S. Zhong, H. Fu, H. Wang, L. Wu, *Chem. Eng. J.* **2021**, *425*, 131630.
- [5] a) A. Yu, Q. Pan, M. Zhang, D. Xie, Y. Tang, *Adv. Funct. Mater.* **2020**, *30*, 2001440; b) S. Muench, A. Wild, C. Friebel, B. Haupler, T. Janoschka, U. S. Schubert, *Chem. Rev.* **2016**, *116*, 9438–9484; c) R. Long, G.-L. Wang, Z.-L. Hu, P.-F. Sun, L. Zhang, *Rare Met.* **2020**, *40*, 1366–1372.
- [6] a) C. Ding, C. Li, H. Tian, Y. Tong, W. Huang, Q. Zhang, *Batteries & Supercaps* **2022**, *5*, 10.1002/batt.202200160; b) B. Esser, *Org. Mater.* **2019**, *01*, 063–070.
- [7] W. Huang, S. Liu, C. Li, Y. Lin, P. Hu, Z. Sun, Q. Zhang, *EcoMat* **2022**, 10.1002/eom2.12214.
- [8] a) X. Lei, Y. Zheng, F. Zhang, Y. Wang, Y. Tang, *Energy Storage Mater.* **2020**, *30*, 34–41; b) M. D. Hager, B. Esser, X. Feng, W. Schuhmann, P. Theato, U. S. Schubert, *Adv. Mater.* **2020**, *32*, 2000587; c) Z. Lin, J. Xie, B. Zhang, J. Li, J.-N. Weng, R.-B. Song, X. Huang, H. Zhang, H. Li, Y. Liu, Z. J. Xu, W. Huang, Q. Zhang, *Nano Energy* **2017**, *41*, 117–127; d) H. Wang, C.-J. Yao, H.-J. Nie, K.-Z. Wang, Y.-W. Zhong, P. Chen, S. Mei, Q. Zhang, *J. Mater. Chem. A* **2020**, *8*, 11906–11922; e) C.-J. Yao, Z. Wu, J. Xie, F. Yu, W. Guo, Z. J. Xu, D.-S. Li, S. Zhang, Q. Zhang, *ChemSusChem* **2020**, *13*, 2457–2463; f) T. Sun, Z.-J. Li, Y.-F. Zhi, Y.-J. Huang, H. J. Fan, Q. Zhang, *Adv. Funct. Mater.* **2021**, *31*, 2010049; g) J. Xie, W. Chen, G. Long, W. Gao, Z. J. Xu, M. Liu, Q. Zhang, *J. Mater. Chem. A* **2018**, *6*, 12985–12991.
- [9] L. Zhu, G. Ding, L. Xie, X. Cao, J. Liu, X. Lei, J. Ma, *Chem. Mater.* **2019**, *31*, 8582–8612.
- [10] Q. Yu, Z. Xue, M. Li, P. Qiu, C. Li, S. Wang, J. Yu, H. Nara, J. Na, Y. Yamauchi, *Adv. Energy Mater.* **2021**, *11*, 2002523.
- [11] C. Luo, O. Borodin, X. Ji, S. Hou, K. J. Gaskell, X. Fan, J. Chen, T. Deng, R. Wang, J. Jiang, C. Wang, *Proc. Natl. Acad. Sci. USA* **2018**, *115*, 2004–2009.
- [12] K. S. Weeraratne, A. A. Alzharani, H. M. El-Kaderi, *ACS Appl. Mater. Interfaces* **2019**, *11*, 23520–23526.
- [13] Y. Tong, Z. Sun, J. Wang, W. Huang, Q. Zhang, *SmartMat* **2022**, 10.1002/smm.21115.
- [14] a) S. Kandambeth, K. Dey, R. Banerjee, *J. Am. Chem. Soc.* **2019**, *141*, 1807–1822; b) H. Tang, Y. Liang, C. Liu, Z. Hu, Y. Deng, H. Guo, Z. Yu, A. Song, H. Zhao, D. Zhao, Y. Zhang, X. Guo, J. Pei, Y. Ma, Y. Cao, F. Huang, *Nature* **2022**, 10.1038/s41586-022-05295-8.
- [15] S. Xu, H. Dai, S. Zhu, Y. Wu, M. Sun, Y. Chen, K. Fan, C. Zhang, C. Wang, W. Hu, *eScience* **2021**, *1*, 60–68.
- [16] a) J. Xie, F. Yu, J. Zhao, W. Guo, H.-L. Zhang, G. Cui, Q. Zhang, *Energy Storage Mater.* **2020**, *33*, 283–289; b) P. Rohland, E. Schröter, O. Nolte, G. R. Newkome, M. D. Hager, U. S. Schubert, *Prog. Polym. Sci.* **2022**, *125*, 101474.
- [17] G. Zhao, Y. Zhang, Z. Gao, H. Li, S. Liu, S. Cai, X. Yang, H. Guo, X. Sun, *ACS Energy Lett.* **2020**, *5*, 1022–1031.
- [18] V. Singh, J. Kim, B. Kang, J. Moon, S. Kim, W. Y. Kim, H. R. Byon, *Adv. Energy Mater.* **2021**, *11*, 2003735.
- [19] Z. Li, Q. Jia, Y. Chen, K. Fan, C. Zhang, G. Zhang, M. Xu, M. Mao, J. Ma, W. Hu, C. Wang, *Angew. Chem. Int. Ed.* **2022**, 10.1002/anie.202207221.
- [20] H. Li, M. Tang, Y. Wu, Y. Chen, S. Zhu, B. Wang, C. Jiang, E. Wang, C. Wang, *J. Phys. Chem. Lett.* **2018**, *9*, 3205–3211.
- [21] B. Tian, J. Zheng, C. Zhao, C. Liu, C. Su, W. Tang, X. Li, G.-H. Ning, *J. Mater. Chem. A* **2019**, *7*, 9997–10003.
- [22] X. Chen, Y. Li, L. Wang, Y. Xu, A. Nie, Q. Li, F. Wu, W. Sun, X. Zhang, R. Vajtai, P. M. Ajayan, L. Chen, Y. Wang, *Adv. Mater.* **2019**, *31*, e1901640.
- [23] Q. Ma, J. Zheng, H. Kang, L. Zhang, Q. Zhang, H. Li, R. Wang, T. Zhou, Q. Chen, A. Liu, H. Li, C. Zhang, *ACS Appl. Mater. Interfaces* **2021**, *13*, 43002–43010.
- [24] G. Zhao, H. Li, Z. Gao, L. Xu, Z. Mei, S. Cai, T. Liu, X. Yang, H. Guo, X. Sun, *Adv. Funct. Mater.* **2021**, *31*, 2101019.
- [25] H. Dai, J. Zou, Y. Gao, Z. Li, C. Zhang, G. Zhang, X. Wang, C. Wang, *J. Polym. Sci.* **2021**, *60*, 992–1001.
- [26] a) J. Zhang, K. Jia, X. Li, X. Liu, L. Zhu, F. Wu, *J. Mater. Chem. A* **2022**, *10*, 10062–10068; b) F. Xiao, P. Liu, J. Li, Y. Zhang, Y. Liu, M. Xu, *Chem. Commun.* **2022**, *58*, 697–700; c) G. Zhao, Y. Sun, Y. Yang, C. Zhang, Q. An, H. Guo, *EcoMat* **2022**, 10.1002/eom2.12221.
- [27] J. Wang, H. Yao, C. Du, S. Guan, *J. Power Sources* **2021**, *482*, 228931.
- [28] a) S. Xu, H. Li, Y. Chen, Y. Wu, C. Jiang, E. Wang, C. Wang, *J. Mater. Chem. A* **2020**, *8*, 23851–23856; b) B. C. Patra, S. K. Das, A. Ghosh, A. Raj, K. P. Moitra, M. Addicoat, S. Mitra, A. Bhaumik, S. Bhattacharya, A. Pradhan, *J. Mater. Chem. A* **2018**, *6*, 16655–16663.

- [29] C. Wu, M. Hu, X. Yan, G. Shan, J. Liu, J. Yang, *Energy Storage Mater.* **2021**, *36*, 347–354.
- [30] X. X. Luo, W. H. Li, H. J. Liang, H. X. Zhang, K. D. Du, X. T. Wang, X. F. Liu, J. P. Zhang, X. L. Wu, *Angew. Chem. Int. Ed.* **2022**, *61*, e202117661.
- [31] M. Mohammadirodbari, K. Qin, C. Luo, *Batteries & Supercaps* **2022**, *5*, 10.1002/batt.202200021.
- [32] T. Shimizu, N. Tanifuji, H. Yoshikawa, *Angew. Chem. Int. Ed.* **2022**, 10.1002/anie.202206093.
- [33] R. Zhou, Y. Huang, Z. Li, S. Kang, X. Wang, S. Liu, *Energy Storage Mater.* **2021**, *40*, 124–138.
- [34] J. Chu, G. Li, Y. Wang, X. Zhang, Z. Yang, Y. Han, T. Cai, Z. Song, *ACS Appl. Mater. Interfaces* **2022**, *14*, 25566–25575.
- [35] a) Y. Yue, H. Li, H. Chen, N. Huang, *J. Am. Chem. Soc.* **2022**, *144*, 2873–2878; b) F. Jiang, Y. Wang, T. Qiu, G. Yang, C. Yang, J. Huang, Z. Fang, J. Li, *J. Power Sources* **2022**, *523*, 231041; c) Q. Li, H. Wang, H. G. Wang, Z. Si, C. Li, J. Bai, *ChemSusChem* **2020**, *13*, 2449–2456.
- [36] a) Z. Lei, Q. Yang, Y. Xu, S. Guo, W. Sun, H. Liu, L. P. Lv, Y. Zhang, Y. Wang, *Nat. Commun.* **2018**, *9*, 576; b) Y. Zhu, P. Chen, Y. Zhou, W. Nie, Y. Xu, *Electrochim. Acta* **2019**, *318*, 262–271.

Manuscript received: September 20, 2022

Revised manuscript received: December 8, 2022

Accepted manuscript online: December 9, 2022

Version of record online: December 29, 2022